



The stability and electronic structures of Li_2MnO_3 in highly charged states

Jialiang Xu¹, Zhenming Xu², Runxin Ouyang¹, Hong Zhu^{1,a)}

¹ University of Michigan–Shanghai Jiao Tong University Joint Institute, Shanghai Jiao Tong University, Shanghai 200240, China

² College of Materials Science and Technology, Nanjing University of Aeronautics and Astronautics, Nanjing 210016, China

^{a)} Address all correspondence to this author. e-mail: hong.zhu@sjtu.edu.cn

Received: 7 January 2022; accepted: 11 April 2022

The large capacity of batteries is always the fundamental prerequisite for the high mileage of electric vehicles. Lithium-rich layered oxides (LLOs) have a higher capacity than the traditional cathode materials (LiTMO_2 , TM = Transition metal). But the capacity attenuation of LLOs after the first cycle is still a limitation. Therefore, it is necessary to systematically study the oxidation mechanism of Li_2MnO_3 , which is the main component of Li-rich cathode material, at highly charged states. This work shows that $\text{Li}_{2-x}\text{MnO}_3$ with Mn migration ($1.5 \leq x < 2$, 50% Mn atoms in the tetrahedral positions of Li layer and 50% Mn atoms in the octahedral positions of transition metal layer, called LMO-T) has lower formation energy than $\text{Li}_{2-x}\text{MnO}_3$ without Mn migration ($1.5 \leq x < 2$, all Mn atoms in the octahedral positions of transition metal layer, called LMO). When the Li concentration is under 25% (except Li concentration = 18.75%), LMO-T has semiconductor properties similar to the initial Li_2MnO_3 , and O atoms in LMO-T are more stable than those in LMO. O bonded with Mn in octahedral position in LMO-T is still likely oxidized during the charging process. The strength of the Mn–O bond is enhanced through S doping by stabilizing O in LMO-T. LMO-T may be an intermediate phase during the charging process from the perspective of electrochemical stability, electronic structure, and chemical bonds. This work reveals the reasons for the instability of layered cathode materials in the late stage of the charging process and also provides a theoretical basis for the design of new LLO cathode materials by enhancing the Mn–O bonding strengths.

Introduction

The development of the high-energy-density cathode material is of great interest for lithium-ion batteries (LIBs). Recently, lithium-rich layered oxides (LLOs), such as $\text{Li}_{(4-x)/3}\text{Mn}_{(2-2x)/3}\text{TM}_x\text{O}_2$ (TM = Ni, Co, etc.) [1], show high theoretical capacities up to 460 mAh/g. Previous work has shown that the Li-rich cathode materials are generally inhomogeneous and composed of a mixture of Li_2MnO_3 and other traditional Li cathode materials (LiTMO_2 , TM = transition metals, and their mixings) [2]. However, LLOs usually are subjected to severe capacity degradations, especially during the first cycle, compared with the traditional LiTMO_2 cathode materials [3–5].

The degradation of LLOs has been considered to be related to the redox reactions of the O anions, which is accompanied by the formation of peroxy oxygen dimer, the release of O_2 gas, and the migration of the transition metals [6]. The prior studies

have shown that Li_2MnO_3 encounters phase transformations during the charging process, and the structural evolution affects the voltage hysteresis [7]. But the redox mechanism is not fully understood, as well as its correlation with the structural evolution of Li_2MnO_3 is not distinct during charging. It has been previously reported that the localized holes on oxygen atoms are critical to the formation of peroxide-like species, such as O^- , O_2^- and O_2^{2-} , but these configurations are not stable and would eventually form molecular O_2 , which would come out of cathode or stay in bulk [6, 8].

Moreover, it has been theoretically reported that octahedral Mn atoms in the transition metal layer migrate to the tetrahedral sites in the Li layer during the charging process [9–11]. The formation of MnO_4 tetrahedron was observed in the $\text{Li}_{0.5}\text{MnO}_3$ structure after 6 ps AIMD at 1000 K from Zhang's work [11]. However, there is no direct experimental evidence to prove the

presence of tetrahedral manganese in the delithiated structure. Thus, the delithiated Li_2MnO_3 with the tetrahedral Mn is reported in some recent works as an intermediate transition product [6, 12, 13]. For example, Radin et al. apply first-principles calculations and show that some Mn atoms migrate from the octahedral sites in the transition metal layer to the neighboring tetrahedral positions in the Li layer, and the Mn^{4+} cations are oxidized to Mn^{7+} [10]. Mn^{6+} and Mn^{7+} in $\text{Li}_{0.5}\text{MnO}_3$ are also observed by AIMD at 1000 K [11]. Vinkeviciute et al. argue that the Mn redox reactions have two steps (Mn^{4+} first oxidized to $\text{Mn}^{7+}/\text{Mn}^{6+}$ and then $\text{Mn}^{7+/6+}$ reduced to Mn^{4+}) and Mn^{7+} ions migrate from the tetrahedral sites in the Li layer back to the octahedral sites in the transition metal layer with the formation of the trapped O_2 [9]. Up to now, far too little attention has been paid to the oxidation mechanism and structural transformation of Li_2MnO_3 upon Li extraction more than 75%, which is essential to improve capacity utilization.

This work studies the structure, stability, and electronic structures of $\text{Li}_{2-x}\text{MnO}_3$ with Mn migration ($1.5 \leq x < 2$, 50% Mn atoms in tetrahedral positions of Li atoms layer and 50% Mn atoms in the octahedral positions of transition metal layer, called LMO-T) and without Mn migration ($1.5 \leq x < 2$, all Mn atoms in the octahedral positions of transition metal layer, called LMO) during the late-charging process. We show that when the Li extraction concentration is more than 75%, LMO-T containing tetrahedral Mn is more stable than LMO and O bonding with Mn in octahedral position affects the stability of LMO and LMO-T. S-doping would further enhance the bonding strength of the octahedral Mn ions and the O ions in LMO-T compared to the undoped material in the late-charging process.

Results and discussion

The stability of Li_2MnO_3 during the late charging process

It has been reported that during the late-charging process of Li_2MnO_3 , especially when the Li concentration is lower than ~25%, the charging voltage of Li_2MnO_3 will increase to 4.8 V [7], and the layered structure will change to the non-layered spinel structure [7]. The formation of spinel LMO is believed to be related to the migration of Mn from the transition metal layer to the Li layer [14]. Thus, in this work, we first assess the thermodynamic stabilities of LMO and LMO-T, whose crystal structures are shown in Fig. 1(a). The top panel of Fig. 1(a) shows the layered Li_2MnO_3 structures, namely LMO, and the bottom panel of Fig. 1(a) shows the non-layered Li_2MnO_3 with Mn in tetrahedral positions of Li layer, namely LMO-T. We analyze the distortions of Mn–O polyhedrons using the continuous symmetry measures (CMS) [15, 16], as shown in Supplementary Table S2. It can be noted that during the delithiation process, the MnO_6 octahedrons in LMO do not have significant distortions

till the Li concentration is lower than 6.25% ($\text{Li}_{0.125}\text{MnO}_3$). Meanwhile, the MnO_6 octahedron and MnO_4 tetrahedron in LMO-T do not experience significant distortions upon the extraction of Li, while the MnO_6 octahedron has a slightly larger distortion compared to that in LMO.

Figure 1(b) shows the calculated formation energies of two phases, each defined by the lowest-energy configurations within our calculations, as shown in Supplementary Table S1. Similar to other researches, we also evaluated the formation energy (E_f) of LMO and LMO-T, following the equation below [17]:

$$E_f = E(\text{Li}_{2-x}\text{MnO}_3) - \left(1 - \frac{x}{2}\right)E(\text{Li}_2\text{MnO}_3) - \frac{x}{2}E(\text{MnO}_3) \quad (1)$$

where $E(\text{Li}_{2-x}\text{MnO}_3)$, $E(\text{Li}_2\text{MnO}_3)$ and $E(\text{MnO}_3)$ are the DFT energies of the delithiated and perfect O3- Li_2MnO_3 and O3- MnO_3 , respectively. As shown in Fig. 1(b), we can see that the formation energy of LMO-T is lower than that of LMO. The difference between the formation energies of LMO and LMO-T increases with the delithiation process. This phenomenon indicates that it is energetically favored for octahedral Mn in the transition metal layer to migrate towards the tetrahedral sites in the lithium layer upon the extraction of Li in Li_2MnO_3 .

It had been reported that there is an unusual behavior of Li_2MnO_3 , a 4.5 V ‘activation’ plateau during the first charge in experiments [18]. To assess the relationship between the migration of Mn and the voltage plateau, we calculated the charging voltages of the LMO and LMO-T systems, as shown in Fig. 1(c). The calculated voltages of $E(\text{Li}_y\text{MnO}_3)$, $y = 2 - x$ were obtained according to Eq. 2 [19].

$$V(y_1) = \frac{E(\text{Li}_{y_1}\text{MnO}_3) - E(\text{Li}_{y_2}\text{MnO}_3) - (y_1 - y_2)E(\text{Li})}{zF} \quad (2)$$

It is interesting that the voltages of LMO-T for late charging process fluctuate between 4.3 and 4.5 V. The voltage of $\text{Li}_{0.5}\text{MnO}_3$ -T (4.39 V) is similar to the result 4.34 V reported in the Radin’s work [10]. Both of them are lower than the experimental results. The voltage is predicted to increase slightly from 4.39 V in $\text{Li}_{0.5}\text{MnO}_3$ to 4.47 V in $\text{Li}_{0.375}\text{MnO}_3$ (with Li concentration is 17.25%), which is in an agreement with the experimental voltage curve for 75–80% extracted lithium (~ $\text{Li}_{0.375}\text{MnO}_3$) [20] and around 80% of Li atoms were extracted during the experiment. Similar steady or slightly fluctuated voltage has been reported in the Li_2MnO_3 - LiNiO_2 Li-rich cathode when Li concentration was lower than 20% [21]. But the voltages of LMO (Li concentration = 25%, 18.75%, and 12.5%, corresponding to $\text{Li}_{0.5}\text{MnO}_3$, $\text{Li}_{0.375}\text{MnO}_3$, and $\text{Li}_{0.25}\text{MnO}_3$, respectively) are higher than 4.8 V.

In general, these results indicate that for Li concentration lower than 25% LMO-T is more stable than LMO in thermodynamics, which is consistent with the previous study that

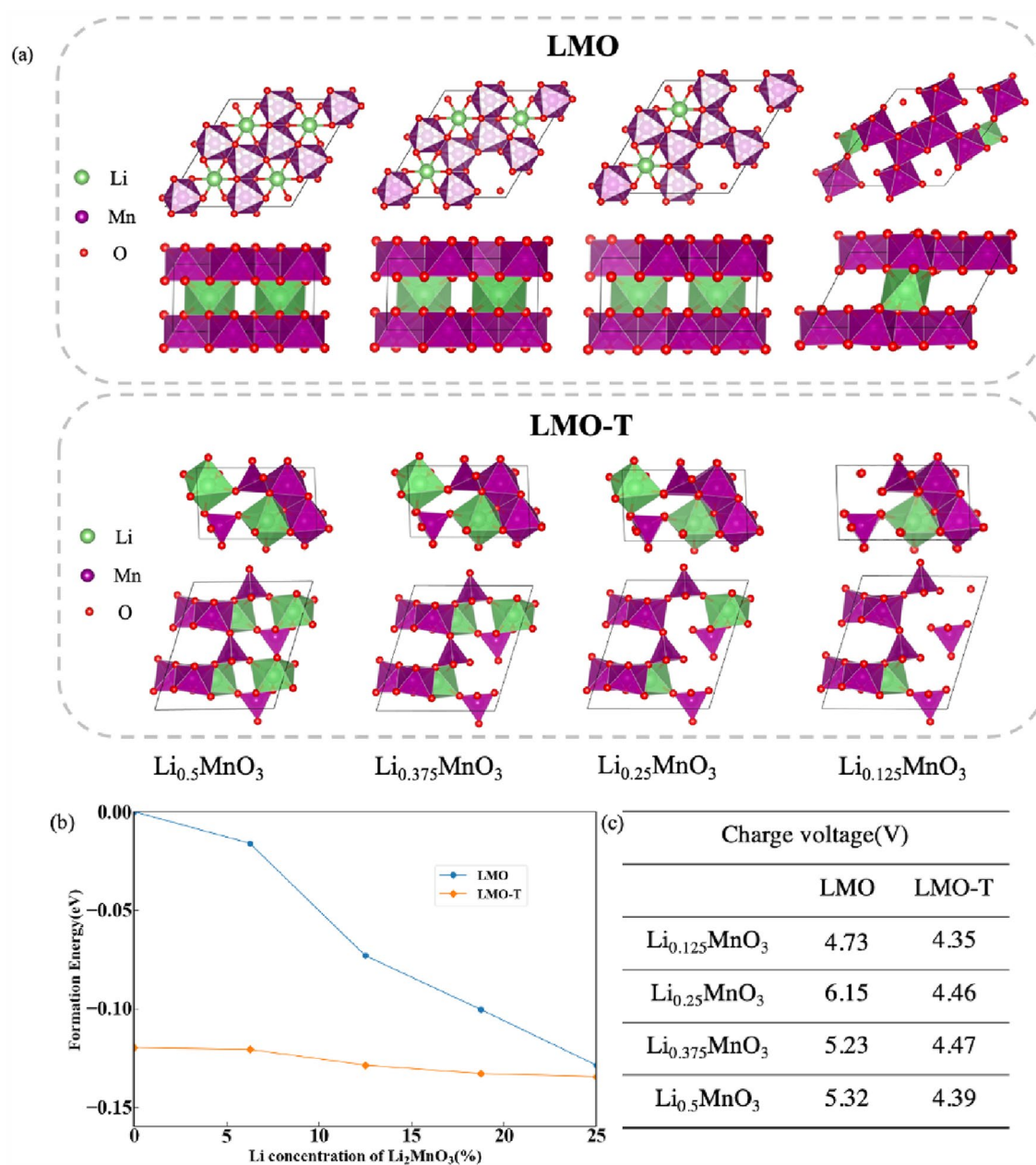


Figure 1: The stability of $\text{Li}_{2-x}\text{MnO}_3$ ($1.5 \leq x < 2$). (a) The crystal structure of LMO (top panel) and LMO-T (lower panel). The green, purple and red spheres represent lithium, manganese, and oxygen ions. (b) The formation energy of LMO and LMO-T. (c) Calculated voltage of LMO and LMO-T.

in $\text{Li}_{0.5}\text{MnO}_3$ there is the phase transformation from LMO to LMO-T [10]. Julija's study showed Li_2MnO_3 underwent a transformation from LMO to LMO-T phase under the $\text{Li}_{0.5}\text{MnO}_3$ composition, and the LMO-T phase changed to a new structure in the discharge process. Mn ions move from the tetrahedral sites to other octahedral sites in the transition metal layer when Mn ions have the secondary migration. As mentioned in the literature, Mn is not observed in the tetrahedral position of the final structure in the experimental works. So LMO-T is an intermediate phase during delithiation. In

addition, a small amount of distorted layered structure existed in the cathode, which affected the voltage during the late-charging process.

Redox mechanism of O oxidation in Li_2MnO_3 during delithiation

Prior studies of Li-rich cathode materials reported that the O anions with the local Li-O-Li configuration in Li_2MnO_3 change the local environment and electrochemical activity

upon charging [22]. The density of states (DOS) of LMO and LMO-T are examined in this work (Supplementary Fig. S2), revealing that LMO is metallic when Li concentration is under 25%, while the LMO-T with the same Li concentration is mainly semiconducting (except Li concentration of 18.75%).

To investigate the oxygen redox reactions and the electrochemical activity of O ions in Li_2MnO_3 , we study the electronic structures and local environments of O ions with different local environments, as shown in Fig. 2. The initial Li_2MnO_3 before charging is reported to have a band-gap of ~ 2.1 eV. [23] It is shown that for $\text{Li}_{0.5}\text{MnO}_3$ of LMO [Fig. 2(a, j)], O(2p) lone-pair band is above Fermi level (marked with the red dashed line). In contrast with O in LMO, the energy of O(2p) orbital in $\text{Li}_{0.5}\text{MnO}_3$ of LMO-T is below the Fermi level [Fig. 2(e, l)], which is probably a result of the migration of Mn atoms. It can then be concluded that the O(2p) orbital of LMO has a higher energy level than that of LMO-T, suggesting that the O are more easily to be oxidized during the charging process. The oxidation of O ions is reported to be responsible for the phase transformation and makes the Li_2MnO_3 unstable [14]. Compared to LiMnO_2 , Li_2MnO_3 has two splitting isolated O(2p) orbitals (b and b^* , b^* higher than b) because of the Li–O–Li configuration [24]. The b orbitals exist along with the Li–O–Li bonding direction and the cationic vacancies also influence the energy of b^* orbitals [25]. The energies of b^* orbitals in Li_2MnO_3 are under the Fermi level [24]. The cationic vacancies in Li_2MnO_3 result in reduced bonding along the Li–O–Li and Li–O–Mn directions. So, the energy of the two 2p orbitals increases until part of them is higher than the Fermi level. As the charging process continues, the number of $\cdot\text{O}\text{--Mn}$ increases (\cdot represents cationic vacancies), and the energy level of b rises until the b orbital and b^* orbital combine around Fermi energy in LMO [Fig. 2(a–d)].

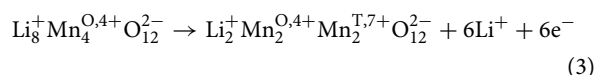
When Mn ions migrate from octahedral positions in the transition metal layer to tetrahedral sites in the Li layer, Mn ions are oxidized from inactive Mn^{4+} to Mn^{7+} to compensate for the loss of positive charge caused by deintercalation of lithium, which is indicated by the magnetic moments of Mn ions [26] in Fig. S1 in the SI. As manganese migrates, there are three kinds of oxygen atoms with the various local environments, resulting in different oxygen activities. O atoms in LMO and LMO-T bonding with Mn at the octahedral position are named O_i , O atoms in LMO-T bonding with Mn at the tetrahedral positions are named O_{ii} , and O atoms in LMO-T bonding with Mn at the octahedral and tetrahedral positions simultaneously are named O_{iii} . It is directly observed in Fig. 2(f–h) that when lithium concentration is lower than 18.75% ($\text{Li}_{0.375}\text{MnO}_3$, $\text{Li}_{0.25}\text{MnO}_3$, $\text{Li}_{0.125}\text{MnO}_3$), the O(2p) orbital splits into two peaks in LMO-T. In addition, the increase in the number of $\cdot\text{O}\text{--Mn}$ raises the b^* energy level. As shown in Fig. 2(f–h), the O(2p) orbital splits

into two orbitals in LMO-T when the lithium concentration is below 18.75%. LMO-T is more stable than LMO when the Li concentration is lower than $\sim 25\%$ based on the analysis of electronic structures. This result is also consistent with the previous work by Radin's [10].

According to the local coordination of Mn and O atoms in LMO and LMO-T, after Mn migration, the binding mode of Mn and O is transformed from octahedron complex MO_6 into tetrahedral complexes MO_4 . To distinguish the activity of O in MO_4 and MO_6 , we studied the DOS of O anions at different positions in LMO and LMO-T using PBE+U, as shown in Fig. 3. O_i in LMO and LMO-T has different activities around the Fermi level. The PDOS of O_i in the LMO passes through the Fermi energy (denoted as 0 eV), while the PDOS of O_i in $\text{Li}_{0.5}\text{MnO}_3$ for LMO-T is under Fermi energy and hence has better electrochemical stability than the former. The PDOS of O_i in others structures ($\text{Li}_{0.375}\text{MnO}_3$, $\text{Li}_{0.25}\text{MnO}_3$ and $\text{Li}_{0.125}\text{MnO}_3$) of LMO-T and LMO has the same regularity as the electronic structures of O in Fig. 2. The PDOS of O_{ii} and O_{iii} of LMO-T do not appear near the Fermi level. Therefore, we observe that O_i is likely to be responsible for the activity of O in LMO-T. This view is echoed that the O_2 is produced and released in phase transformation during the late delithiation [27]. Upon the lithium extraction, the amount of $\cdot\text{O}\text{--Mn}$ increases and the DOS for O_{ii} and O_{iii} do not vary obviously, indicating the stability of O_{ii} and O_{iii} . Therefore, it is feasible to dope with other elements to enhance the Mn–O (especially the Mn– O_i) bond and reduce the possibility of oxygen releasing in LMO-T.

Charge transfer with phase transformation in Li_2MnO_3

Li_2MnO_3 is considered stable but electrochemically inactive due to the presence of Mn^{4+} . When Mn migrating from octahedral position to tetrahedral position, 50% of Mn^{4+} ions convert to Mn^{7+} , and the chemical equilibrium is as follows,



To further investigate oxygen reactions after Mn migration, the Bader charge of O and Mn ions in $\text{Li}_{0.5}\text{MnO}_3$ is evaluated by its electron transferability. We calculated the Bader charge of O and Mn ions in $\text{Li}_{0.5}\text{MnO}_3$ in different local environments (Table 1), showing that Bader charges within LMO and LMO-T are distinct. O_i in LMO-T is more negatively charged and hence more stable than O_i in LMO, which is consistent with the DOS analysis in the previous section. The Mn in tetrahedral position, named Mn_{tet} , is more positively charged than Mn_{oct} . The $\text{Mn}_{\text{tet}}\text{--O}$ bond is more stable than $\text{Mn}_{\text{oct}}\text{--O}$ bond in LMO-T. Moreover, since the Mn_{oct} bonds with O_i and O_{iii} in LMO-T but only bonds with O_i in LMO, the Bader charge around Mn_{oct} differs in LMO and LMO-T. The length of the $\text{Mn}_{\text{oct}}\text{--O}_{iii}$

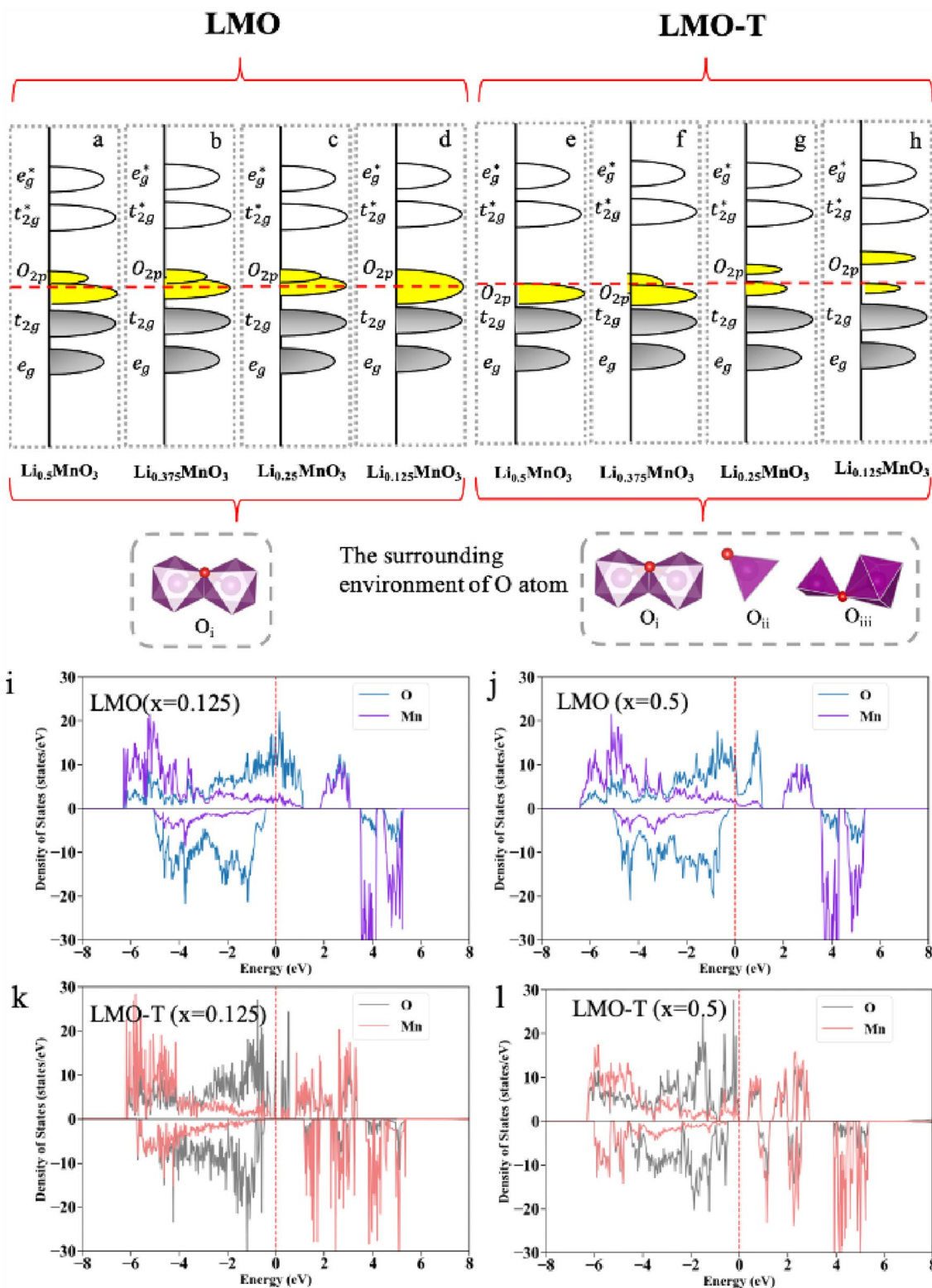


Figure 2: The electronic structures and local environments of O atoms in LMO and LMO-T. (a–h) The schematic draw about the electronic structures. The hollow black area, filled yellow region, and filled gray represent the empty antibonding (M–O)* states, O(2p) lone-pair states, and bonding (M–O) states, respectively. The manganese and oxygen ions are shown in purple and red, respectively. (i–l) The DOS of Mn and O for LMO and LMO-T ($Li_{0.5}MnO_3$ and $Li_{0.125}MnO_3$).

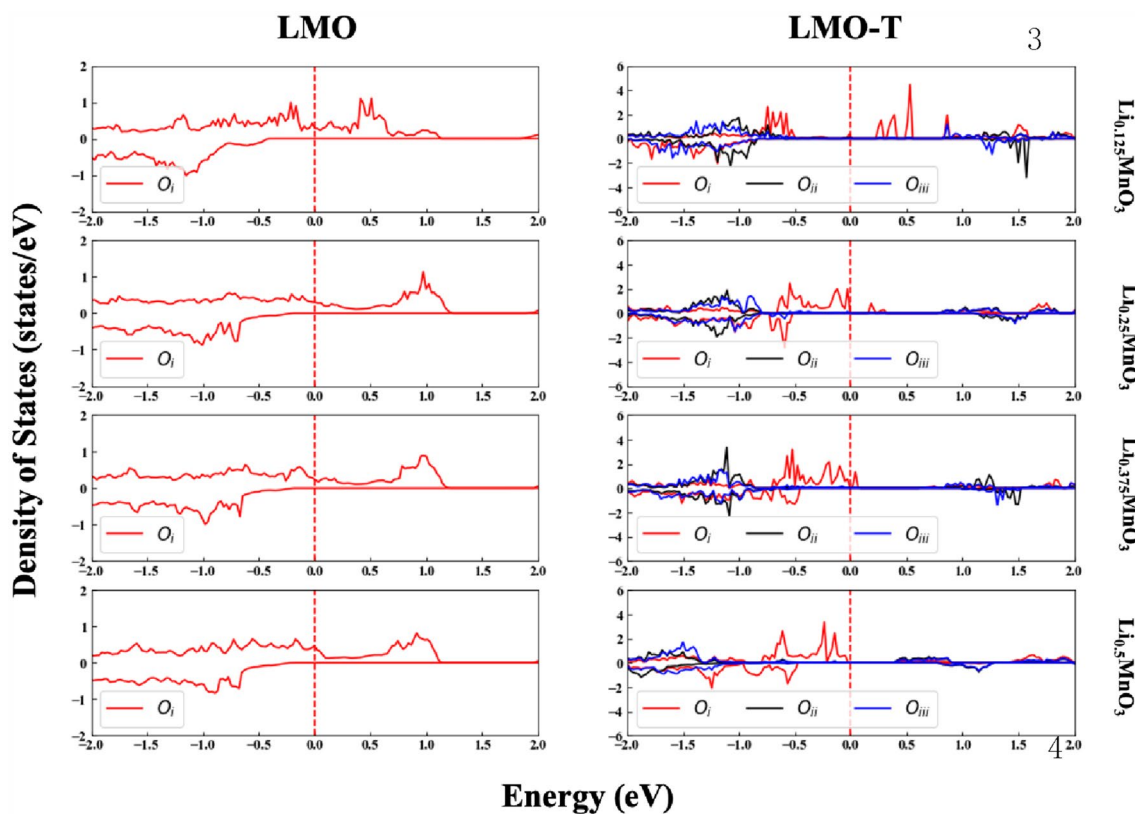


Figure 3: Project density of state (PDOS) of LMO and LMO-T. The O_i (bonding with Mn in octahedral position) in the LMO and LMO-T; O_{ii} (bonding with Mn in tetrahedral positions) and O_{iii} (bonding both with Mn in octahedral position and tetrahedral position) in the LMO-T.

TABLE 1: The Bader charge (e) of $\text{Li}_{0.5}\text{MnO}_3$ in LMO and LMO-T structures.

Atomic species	LMO	LMO-T
O_i	0.7795	0.9219
O_{ii}	\	0.6268
O_{iii}	\	0.7739
Mn_{oct}	-1.8907	-1.8367
Mn_{tet}	\	-1.9047

Positive (negative) Bader charge values represent negatively (positively) charged ions.

bond in LMO-T is 2.11–2.17 Å longer than the $\text{Mn}_{\text{oct}}\text{-O}_i$ bond 1.93–1.95 Å in LMO. But the length of the $\text{Mn}_{\text{oct}}\text{-O}_i$ bond in LMO-T is 1.85–1.90 Å, shorter than the $\text{Mn}_{\text{oct}}\text{-O}_i$ bond in LMO. It could be concluded from the above results that the $\text{Mn}_{\text{oct}}\text{-O}_i$ bond in LMO-T is more stable than that in LMO.

To quantify the charge state of O during delithiation, we further calculated the Bader charge of O and Mn atoms for LMO and LMO-T phase at four delithiated states and analyzed the atomic charge difference of $\text{Li}_{0.375}\text{MnO}_3$, $\text{Li}_{0.25}\text{MnO}_3$ and $\text{Li}_{0.125}\text{MnO}_3$ with respect to those of $\text{Li}_{0.5}\text{MnO}_3$ (shown in Fig. 4). A negative (positive) value for the change of Bader charge (with respect to $\text{Li}_{0.5}\text{MnO}_3$) indicates losing (obtaining) electron of the ions, corresponding to the oxidation (reduction) reaction. The Bader

analysis shows that the oxidation of O with more electron loss dominates the charge compensation of the whole system upon charging. And the value of charge transfer between O atoms with the different Li concentrations is similar between the LMO and LMO-T during the late-charging process seen from Fig. 4.

The reduction of Mn_{oct} in LMO indicated that O is activated. The oxidation of Mn_{oct} in LMO-T during delithiation is surprising. It is likely that after Mn migration from octahedral position to tetrahedral position, the MO_6 is distorted, and the strength of the Mn–O bond is changed. When lithium concentration is equal to 25.0%, the charge transfer of Mn in tetrahedral position in LMO-T is significantly different from that at 18.75%.

This result may be explained that the LMO-T is not the most stable structure and will continue change to another phase. These charge transfer analyses may also show that LMO-T is more stable than LMO, which is consistent with the results of electronic structures.

Doping of S stabilizes O_i in LMO-T

O_i is excessively oxidized upon the generation of lithium vacancies and the local environment change of Mn. Our goal is to introduce new kinds of anions to combine with Mn and

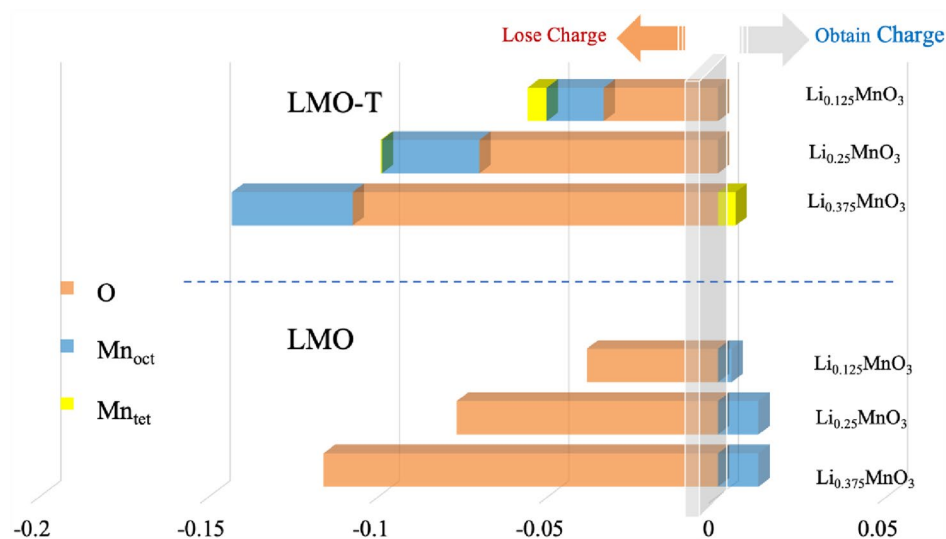


Figure 4: Bader analysis of the Mn and O ions for LMO and LMO-T phase in different delithiation states. Mn_{oct} represents Mn in octahedral position, Mn_{tet} represents Mn in tetrahedral position. All the value is the difference compare to Li_{0.5}MnO₃ in LMO and LMO-T. A negative value indicates electron loss at the ions, corresponding to the oxidation reaction. A positive value indicates electron gain at the ions, corresponding to the reduction reaction.

reduce O activity. The inductive effect in polyanion compounds achieves the effect of stabilizing oxygen mentioned in the early work [28].

Sulfur (4.17%) atom is utilized to stabilize O_i in Li₂MnO₃ [25, 29]. LMO-T has three kinds of O sites shown in Fig. 2. The doping energy of S at the O_i position is lower than that at O_{ii} by 0.069 eV per formula (at O_{iii} by 0.030 eV per formula). So, the S appearing at O_i position of LMO-T is the most stable structure. After doping S, the strength of the Mn–S bond is weaker than the Mn–O bond and impacts other surrounding Mn–O bonds. Then, we dope LMO and LMO-T with the S element, replacing an O_i atom with the S atom. The structures and DOS of LMO and LMO-T after doping an S are compared in Fig. 5. After structural optimization, we find that the shape of the LMO unit cell does not change significantly, but the lattice constants increase and the volume of the cell also raises.

The volume expansion of LMO upon S doping increases from to 14.87% during the late charging stage considered in this work (Supplementary Table S3). As shown in Fig. 5(a), when lithium concentration is lower than 25%, the local structure changes significantly near the doped S atom, forming a small polarization tetrahedral molecular structure of (SO₃)^{x-}. S replaces O_i and combines with Mn in Li_{0.5}MnO₃ without forming (SO₃)^{x-}.

Red solid lines represent the DOS for the Mn element, and black dashed lines denote the DOS of the neighboring O element in Fig. 5. In LMO (Li concentration = 25%, 18.75%, and 12.5%), after S doping Mn and O have weak hybridization, the electrons of O ions are easy to be oxidized up to empty O(2p) orbitals. When Li concentration is 6.25%, the hybridization

between Mn and O is enhanced. As shown in Fig. 5(b), S replaces O to bond with Mn forming an Mn–S bond which does not activate the inductive effect in polyanionic LMO-T. LMO-T (Li concentration = 18.75%) displays semiconductor-like properties in Fig. 5(b). When Li concentration lower than 12.5%, Mn and O has strong hybridization than Mn–O bond before S doping in LMO-T (as shown in Fig. 2). According to these data, we infer that the distortion of Mn octahedron induced by doping with S enhances the Mn–O bond and stabilizes O_i in LMO-T. But the effect of doping S is unobvious in LMO. It is argued that doping S anions stabilizes O_i in LMO-T and reduces the possibility of O releasing. Compared with the results in Supplementary Fig. S4, the average length of the Mn–S bond is 2.316 Å in LMO-T after doping, longer than the Mn–O bond (1.876 Å) in LMO-T without doping. The Mn–S bond causes the distortion of the surrounding MnO₅S octahedron and MnO₆ octahedron, because the S has a larger atomic radius than O. This finding has the implications for developing a new method of doping anions (such as S) in Li₂MnO₃ to reduce the O activity and hence the phase transformation.

Conclusion

We investigate the structural stabilities and redox mechanisms of LMO-T and LMO during the late-charging process based on first-principles calculations. This study shows that the new phase LMO-T is generated by Mn in an octahedral position of transition metal layer migrating to the tetrahedral sites in the lithium layer. LMO-T is more stable than LMO during delithiation, showing semiconductor-like properties, similar to the initial

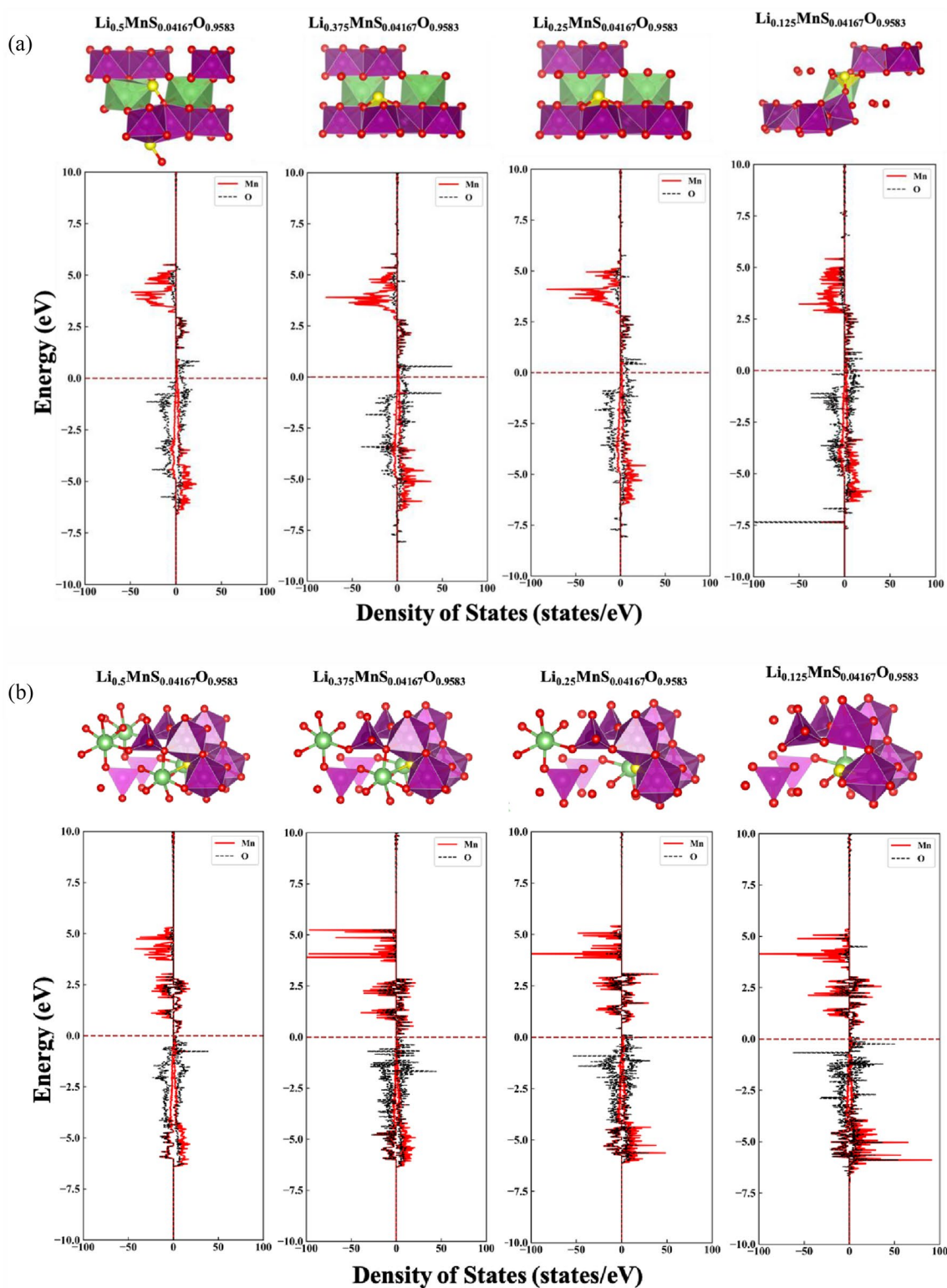


Figure 5: The structures and DOS with sulfur doping in LMO and LMO-T. (a) Crystal structure and DOS for the total and elements of LMO with S doping. (b) Crystal structure and DOS of LMO-T with S doping. The green, purple, red, and yellow spheres represent lithium, manganese, oxygen, and S ions.

material Li_2MnO_3 . Different from LMO-T, the LMO has metallic properties upon delithiation, which may be related to the formation of $\cdot\cdot\text{O}-\text{Li}$ and $\cdot\cdot\text{O}-\text{Mn}$ structures and the high oxidation

state of Mn ions. When the Li concentration is lower than 25%, O_i in LMO-T is easily oxidized. Bader charge analysis indicates Mn_{oct} in different phases has opposite oxidation-reduction

behavior. And the doping of the anion S enhances the strength of the Mn–O bond, stabilizes the O_p , potentially reduces the release of oxygen in LMO-T, and improves the stability of Li_2MnO_3 . According to this work, anions could be doped into cathode materials when designing a high-capacity cathode.

Materials and methods

The density functional theory (DFT) [30] calculations were performed by using the Projector-Augmented Wave (PAW) method [31, 32] implemented in Vienna ab Initio Simulation Package (VASP) [33]. The Perdew–Burke–Ernzerhof (PBE) [34] version of the generalized gradient approximation (GGA) is chosen for all the calculations [35, 36]. The effective on-site Hubbard U_{eff} correction on the 3d or 4d electrons for all the transition metals is included in our calculations. In this work, U parameter of 3.9 eV and 5.0 eV on Mn in Li_2MnO_3 were applied for energy and DOS calculations, respectively [10, 19, 37]. It has been reported before that when the U value of Mn is 3.9 eV ($J = 1$ eV), the formation energy of the PBE+ U method is similar to that of other methods (HSE and SCAN) [10]. When we calculate the density of states (DOS), the 5.0 eV of U value has been used, which was theoretically estimated for Mn^{4+} in spinel-type MnO_2 [37]. Our calculated DOS of $Li_{0.5}MnO_3$ in LMO-T is similar to that in Radin's work [10]. Xiao [23] has calculated the band structure of Li_2MnO_3 with GGA+ U ($U = 5.0$ eV) and predicted an indirect band gap of ~ 2.1 eV, close to the experimental optical band gap determined by X-ray photoelectron spectroscopy (XPS). The cutoff energy of the plane-wave basis set was 500 eV. The Gamma-centered grids $2 \times 2 \times 5$ k -point mesh was applied for integration in the Brillouin zone of LMO, while $2 \times 5 \times 2$ k -point mesh was employed for LMO-T. Cell parameters and atomic positions were fully relaxed for bulk calculations. All calculations were converged to 10^{-5} eV/atom for total energy and below 0.02 eV/Å for interatomic forces. Delithiated Li_2MnO_3 was modeled by using a $2 \times 2 \times 1$ supercell. For a specific lithium concentration, the structure of LMO with the lowest DFT energy was adopted for further analyses, as shown in Supplementary Table S1 [38]. The initial structure of $Li_{0.5}MnO_3$ in LMO-T was adopted from Radin et al.'s work [10]. Data processing and structure visualization were performed based on the pymatgen package [39] and VESTA software [40].

Acknowledgments

This work was supported by the National Natural Science Foundation of China (51602196, 52072240), the Shanghai Automotive Industry Corporation (1714), and the Materials Genome Initiative Center at Shanghai Jiao Tong University. All

simulations were performed at the Shanghai Jiao Tong University High Performance Computing Center.

Declarations

Conflict of interest The authors declare no competing financial interest.

Supplementary Information

The online version contains supplementary material available at <https://doi.org/10.1557/s43578-022-00563-9>.

References

1. K. Nakayama, R. Ishikawa, S. Kobayashi, N. Shibata, Y. Ikuhara, Dislocation and oxygen-release driven delithiation in Li_2MnO_3 . *Nat. Commun.* **11**(1), 4452 (2020). <https://doi.org/10.1038/s41467-020-18285-z>
2. M.M. Thackeray, S.-H. Kang, C.S. Johnson, J.T. Vaughey, R. Benedek, S.A. Hackney, Li_2MnO_3 -stabilized $LiMO_2$ ($M = Mn, Ni, Co$) electrodes for lithium-ion batteries. *J. Mater. Chem.* **17**(30), 3112 (2007). <https://doi.org/10.1039/b702425h>
3. R.N. Ramesha, C.P. Laisa, K. Ramesha, Improving electrochemical stability by transition metal cation doping for manganese in lithium-rich layered cathode, $Li_{1.2}Ni_{0.13}Co_{0.13}Mn_{0.54-x}M_xO_2$ ($M = Co, Cr$ and Fe). *Electrochim. Acta* **249**, 377–386 (2017). <https://doi.org/10.1016/j.electacta.2017.08.039>
4. C. Yin, L. Wan, B. Qiu, F. Wang, W. Jiang, H. Cui, J. Bai, S. Ehrlich, Z. Wei, Z. Liu, Boosting energy efficiency of Li-rich layered oxide cathodes by tuning oxygen redox kinetics and reversibility. *Energy Storage Mater.* **35**, 388–399 (2021). <https://doi.org/10.1016/j.ensm.2020.11.034>
5. J.-L. Shi, D.-D. Xiao, X.-D. Zhang, Y.-X. Yin, Y.-G. Guo, L. Gu, L.-J. Wan, Improving the structural stability of Li-rich cathode materials via reservation of cations in the Li-slab for Li-ion batteries. *Nano Res.* **10**(12), 4201–4209 (2017). <https://doi.org/10.1007/s12274-017-1489-3>
6. H. Chen, M.S. Islam, Lithium extraction mechanism in Li-rich Li_2MnO_3 involving oxygen hole formation and dimerization. *Chem. Mater.* **28**(18), 6656–6663 (2016). <https://doi.org/10.1021/acs.chemmater.6b02870>
7. M. Oishi, K. Shimoda, K. Ohara, D. Kabutan, T. Kawaguchi, Y. Uchimoto, Disordered cubic spinel structure in the delithiated Li_2MnO_3 revealed by difference pair distribution function analysis. *J. Phys. Chem. C* **124**(44), 24081–24089 (2020). <https://doi.org/10.1021/acs.jpcc.0c07124>
8. A.S. Tygesen, J.H. Chang, T. Vegge, J.M. García-Lastra, Computational framework for a systematic investigation of anionic redox process in Li-rich compounds. *npj Comput. Mater.* **6**(1), 65 (2020). <https://doi.org/10.1038/s41524-020-0335-4>

9. J. Vinckeviciute, D.A. Kitchaev, A. Van der Ven, A two-step oxidation mechanism controlled by Mn migration explains the first-cycle activation behavior of Li_2MnO_3 -based Li-excess materials. *Chem. Mater.* **33**(5), 1625–1636 (2021). <https://doi.org/10.1021/acs.chemmater.0c03734>
10. M.D. Radin, J. Vinckeviciute, R. Seshadri, A. Van der Ven, Manganese oxidation as the origin of the anomalous capacity of Mn-containing Li-excess cathode materials. *Nat. Energy* **4**(8), 639–646 (2019). <https://doi.org/10.1038/s41560-019-0439-6>
11. Z. Zhang, S. Zhao, B. Wang, H. Yu, Local redox reaction of high valence manganese in Li_2MnO_3 -based lithium battery cathodes. *Cell Rep. Phys. Sci.* **1**(5), 100061 (2020). <https://doi.org/10.1016/j.xcrp.2020.100061>
12. J.-X. Wang, Structure and delithiation/lithiation of the lithium-rich layered oxide as cathode material. *Int. J. Electrochem. Sci.* (2017). <https://doi.org/10.20964/2017.09.25>
13. E. Lee, K.A. Persson, Structural and chemical evolution of the layered Li-excess Li_xMnO_3 as a function of Li content from first-principles calculations. *Adv. Energy Mater.* **4**(15), 1400498 (2014). <https://doi.org/10.1002/aenm.201400498>
14. J.-M. Lim, D. Kim, Y.-G. Lim, M.-S. Park, Y.-J. Kim, M. Cho, K. Cho, The origins and mechanism of phase transformation in bulk Li_2MnO_3 : first-principles calculations and experimental studies. *J. Mater. Chem. A* **3**(13), 7066–7076 (2015). <https://doi.org/10.1039/C5TA00944H>
15. D. Waroquiers, X. Gonze, G.-M. Rignanese, C. Welker-Nieuwoudt, F. Rosowski, M. Göbel, S. Schenk, P. Degelmann, R. André, R. Glaum, G. Hautier, Statistical analysis of coordination environments in oxides. *Chem. Mater.* **29**(19), 8346–8360 (2017). <https://doi.org/10.1021/acs.chemmater.7b02766>
16. M. Pinsky, D. Avnir, Continuous symmetry measures. 5. The classical polyhedra. *Inorg. Chem.* **37**(21), 5575–5582 (1998). <https://doi.org/10.1021/ic9804925>
17. M. Zheng, Z. Bai, Y.-W. He, S. Wu, Y. Yang, Z.-Z. Zhu, Anionic redox processes in maricite- and triphylite- NaFePO_4 of sodium-ion batteries. *ACS Omega* **5**(10), 5192–5201 (2020). <https://doi.org/10.1021/acsomega.9b04213>
18. J. Rana, M. Stan, R. Kloepsch, J. Li, G. Schumacher, E. Welter, I. Zizak, J. Banhart, M. Winter, Structural changes in Li_2MnO_3 cathode material for Li-ion batteries. *Adv. Energy Mater.* **4**(5), 1300998 (2014). <https://doi.org/10.1002/aenm.201300998>
19. Y. Koyama, I. Tanaka, M. Nagao, R. Kanno, First-principles study on lithium removal from Li_2MnO_3 . *J. Power Sources* **189**(1), 798–801 (2009). <https://doi.org/10.1016/j.jpowsour.2008.07.073>
20. D.Y.W. Yu, K. Yanagida, Y. Kato, H. Nakamura, Electrochemical activities in Li_2MnO_3 . *J. Electrochem. Soc.* **156**(6), A417–A424 (2009). <https://doi.org/10.1149/1.3110803>
21. T. Ohzuku, M. Nagayama, K. Tsuji, K. Ariyoshi, High-capacity lithium insertion materials of lithium nickel manganese oxides for advanced lithium-ion batteries: toward rechargeable capacity more than 300 MA h G^{-1} . *J. Mater. Chem.* **21**(27), 10179 (2011). <https://doi.org/10.1039/c0jm04325g>
22. D.-H. Seo, J. Lee, A. Urban, R. Malik, S. Kang, G. Ceder, The structural and chemical origin of the oxygen redox activity in layered and cation-disordered Li-excess cathode materials. *Nat. Chem.* **8**(7), 692–697 (2016). <https://doi.org/10.1038/nchem.2524>
23. R. Xiao, H. Li, L. Chen, Density functional investigation on Li_2MnO_3 . *Chem. Mater.* **24**(21), 4242–4251 (2012). <https://doi.org/10.1021/cm3027219>
24. M. Okubo, A. Yamada, Molecular orbital principles of oxygen-redox battery electrodes. *ACS Appl. Mater. Interfaces* **9**(42), 36463–36472 (2017). <https://doi.org/10.1021/acsami.7b09835>
25. Q. Chen, Y. Pei, H. Chen, Y. Song, L. Zhen, C.-Y. Xu, P. Xiao, G. Henkelman, Highly reversible oxygen redox in layered compounds enabled by surface polyanions. *Nat. Commun.* **11**(1), 3411 (2020). <https://doi.org/10.1038/s41467-020-17126-3>
26. J. Reed, G. Ceder, Role of electronic structure in the susceptibility of metastable transition-metal oxide structures to transformation. *Chem. Rev.* **104**(10), 4513–4534 (2004). <https://doi.org/10.1021/cr020733x>
27. A.R. Armstrong, M. Holzapfel, P. Novák, C.S. Johnson, S.-H. Kang, M.M. Thackeray, P.G. Bruce, Demonstrating oxygen loss and associated structural reorganization in the lithium battery cathode $\text{Li}[\text{Ni}_{0.2}\text{Li}_{0.2}\text{Mn}_{0.6}]\text{O}_2$. *J. Am. Chem. Soc.* **128**(26), 8694–8698 (2006). <https://doi.org/10.1021/ja062027+>
28. B.C. Melot, J.-M. Tarascon, Design and preparation of materials for advanced electrochemical storage. *Acc. Chem. Res.* **46**(5), 1226–1238 (2013). <https://doi.org/10.1021/ar300088q>
29. G. Chen, J. An, Y. Meng, C. Yuan, B. Matthews, F. Dou, L. Shi, Y. Zhou, P. Song, G. Wu, D. Zhang, Cation and anion Codoping synergy to improve structural stability of Li- and Mn-rich layered cathode materials for lithium-ion batteries. *Nano Energy* **57**, 157–165 (2019). <https://doi.org/10.1016/j.nanoen.2018.12.049>
30. D.S. Sholl, J.A. Steckel, *Density Functional Theory: A Practical Introduction* (Wiley, Hoboken, 2011)
31. G. Kresse, J. Furthmüller, Efficient iterative schemes for ab initio total-energy calculations using a plane-wave basis set. *Phys. Rev. B* **54**(16), 11169–11186 (1996). <https://doi.org/10.1103/PhysRevB.54.11169>
32. P.E. Blöchl, O. Jepsen, O.K. Andersen, Improved tetrahedron method for Brillouin-zone integrations. *Phys. Rev. B* **49**(23), 16223–16233 (1994). <https://doi.org/10.1103/PhysRevB.49.16223>
33. J. Hafner, Ab-initio simulations of materials using VASP: density-functional theory and beyond. *J. Comput. Chem.* **29**(13), 2044–2078 (2008). <https://doi.org/10.1002/jcc.21057>
34. W. Kohn, L.J. Sham, Self-consistent equations including exchange and correlation effects. *Phys. Rev.* **140**(4A), A1133–A1138 (1965). <https://doi.org/10.1103/PhysRev.140.A1133>

35. S.L. Dudarev, G.A. Botton, S.Y. Savrasov, C.J. Humphreys, A.P. Sutton, Electron-energy-loss spectra and the structural stability of nickel oxide: an LSDA+U study. *Phys. Rev. B* **57**(3), 1505–1509 (1998). <https://doi.org/10.1103/PhysRevB.57.1505>
36. J.P. Perdew, K. Burke, M. Ernzerhof, Generalized gradient approximation made simple [*Phys. Rev. Lett.* **77**, 3865 (1996)]. *Phys. Rev. Lett.* **78**(7), 1396 (1997). <https://doi.org/10.1103/PhysRevLett.78.1396>
37. F. Zhou, M. Cococcioni, C.A. Marianetti, D. Morgan, G. Ceder, First-principles prediction of redox potentials in transition-metal compounds with LDA + U. *Phys. Rev. B* **70**(23), 235121 (2004). <https://doi.org/10.1103/PhysRevB.70.235121>
38. A.Y. Toukmaji, J.A. Board, Ewald summation techniques in perspective: a survey. *Comput. Phys. Commun.* **95**(2–3), 73–92 (1996). [https://doi.org/10.1016/0010-4655\(96\)00016-1](https://doi.org/10.1016/0010-4655(96)00016-1)
39. S.P. Ong, W.D. Richards, A. Jain, G. Hautier, M. Kocher, S. Cholia, D. Gunter, V.L. Chevrier, K.A. Persson, G. Ceder, Python materials genomics (Pymatgen): a robust, open-source python library for materials analysis. *Comput. Mater. Sci.* **68**, 314–319 (2013). <https://doi.org/10.1016/j.commatsci.2012.10.028>
40. K. Momma, F. Izumi, *VESTA 3* for three-dimensional visualization of crystal, volumetric and morphology data. *J. Appl. Crystallogr.* **44**(6), 1272–1276 (2011). <https://doi.org/10.1107/S0021889811038970>